Ocean Modelling 187 (2024) 102306

Contents lists available at ScienceDirect

Ocean Modelling

journal homepage: www.elsevier.com/locate/ocemod

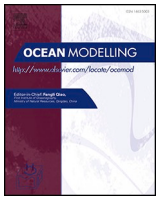

Reynolds-averaged Navier-Stokes simulation of nearshore Langmuir circulation and the formation of oil-particle aggregates

J.J. Peñaloza-Gutierrez [a,*], A.E. Tejada-Martínez [b], M.C. Boufadel [c]

[a] Mechanical Engineering, University of South Florida, Tampa, FL, United States
[b] Civil & Environmental Engineering, University of South Florida, Tampa, FL, United States
[c] Civil and Environmental Engineering, New Jersey Institute of Technology, United States

ARTICLE INFO

Keywords:
Oil spill
Resuspended sediments
Oceanic turbulence
Flocculation
Langmuir supercells
Population balance model

ABSTRACT

Langmuir turbulence in the inner shelf coastal ocean is characterized by Langmuir circulation (LC) or cells that can span the full depth of unstratified water columns. A Reynolds-averaged Navier-Stokes (RANS) simulation strategy resolving full-depth LC coupled with an oil-particle aggregate (OPA) formation model is introduced. It is seen that full-depth LC generated by wind and waves under storm conditions can result in sediment resuspension and oil droplet entrainment (in the case of an oil spill) and subsequent mixing between these two, leading to significant OPA formation. This conclusion comes from a simulation in which various classes of oil droplets (with diameters ranging between 40 and 140 μm) were released at the surface, each class initialized with a 0.1 kg m^{-3} concentration. The full-depth LC led to most of the oil becoming trapped within OPAs in the first 5 min. The majority of the larger oil droplets were quickly aggregated with sediments near surface, whereas the smaller oil droplets were first submerged by the downwelling limbs of the Langmuir cells, and eventually aggregated with sediment while being carried upwards by the upwelling limbs. The OPAs conglomerated in the form of clouds transported by the action of the cells, with the heavier OPAs eventually settling within the upwelling limb of the cells while slowly depositing to the bed over time.

1. Introduction

Wave-wind current interaction drives Langmuir turbulence in the coastal ocean (Langmuir, 1938; Thorpe, 2004). Langmuir turbulence is described by a vast scope of Langmuir circulation (LC) scales or cells, parallel counter-rotating vortices oriented approximately in the wind direction and advected by the mean flow. Cells can extend tens of meters to kilometers in the downwind direction, defining the larger spatial scales. The distance between cells can vary from a few meters to up to a kilometer (Thorpe, 2004). LCs possess a downwelling limb (consisting of negative velocity fluctuations) generated by the surface convergence of cell pair, and an upwelling limb (consisting of positive velocity fluctuations) generated by the bottom convergence of each cell pair. These limbs lead to increased levels of mixing in the water column. At the surface convergence of the cells, floating debris (buoyant material) and foam can accumulate, forming rows often referred to as windrows. The surface convergence of the cells is also distinguished by its intense positive downwind velocity fluctuations, which enhances the mean current in that direction.

Langmuir turbulence is generated under favorable conditions when wind speeds are above 3 m s^{-1} and the wind direction is parallel to the waves. When these conditions are met, small LC scales emanate from the water surface, growing in depth and width over time. Commonly, they descend across the mixed layer in the upper ocean (Skyllingstad and Denbo, 1995) or the entire water column in homogenous shallow water, having been observed engulfing a water column of up to 20 m in depth (Savidge and Gargett, 2017).

Gargett et al. (2004) and Gargett and Wells (2007) recorded extended occurrences of full-depth LC lasting more than 20 h during the passage of a storm over which the cells evolved having widths (down-well-to-downwell distances (Fig. 1)) of up to 4 times the water column depth. They denoted these cells as Langmuir supercells (LS) due to their important role in transporting sediment and bioactive material on shallow shelves.

Evidence of the presence of LCs close to the shore and their impact on transport across the surf zone has also been given by Chubarenko and Stepanova (2017). They observed the accumulation of negatively buoyant material along slicks aligned with the wind. Slicks were seen

* Corresponding author.
E-mail address: jjpenalozagu@usf.edu (J.J. Peñaloza-Gutierrez).

https://doi.org/10.1016/j.ocemod.2023.102306
Received 4 September 2023; Received in revised form 5 December 2023; Accepted 15 December 2023
Available online 16 December 2023

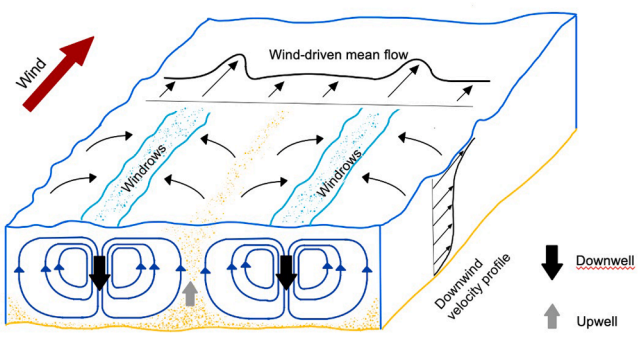

Fig. 1. Sketch of Langmuir cells with wind direction perpendicular to the shore favoring onshore transport. Adapted from Chubarenko and Stepanova (2017).

in-between windrows, nearly perpendicular to the coast. In Fig. 1, following the observations and depiction of Chubarenko and Stepanova (2017), full-depth LCs or LS can be seen just beyond the surf zone region, contributing to the transport of materials from the inner shelf to the beach. As noted by Chubarenko and Stepanova (2017), LCs resuspend material found in the inner shelf seabed and, in combination with the waves and wind, transport suspended material toward the shore along the slicks. Their observations are consistent with those of Gargett et al. (2004), who noted that the strong coherence of LS enables them to efficiently move sediments from the low-speed layer close to the seabed towards the strong and directional mean flow in the downwind direction. Sediments are swept towards the bottom convergence of the cells (i.e., the bottom of the upwelling limbs), inducing sediment resuspension by lifting the particles into the bulk of the water column, resulting in subsequent lateral transport.

Liu et al. (2019) investigated sediment flocculation processes induced by LS in a coastal region by coupling a size-resolving flocculation model with a turbulence-resolving (large-eddy simulation or LES) model. Models that are based on size classes distribute the mass of particles into a set of fixed-size classes to determine the particle population (Verney et al., 2011). According to their findings, LS and its linked Langmuir turbulence keep sediment flocs suspended in the water and arrange flocs by size.

Positively buoyant particles can be entrained and trapped in ocean subsurface regions when the downwelling limbs' vertical speed exceeds the particles' buoyant rise speed. Analogously, negatively buoyant particles can be lifted when upwelling limbs exert greater vertical speeds than the settling speed of the particles. Regions where the limbs can hold material suspended in the water column are known as Stommel Retention Zones or SRZs (Stommel 1949). For example, in oil spills, LCs can entrain and distribute oil droplets throughout the water column, as observed in the simulations conducted by Farmer and Li (1994) and Perez et al. (2021). They showed that the downwelling limbs of LC promote dispersion of oil droplets around the submerged SRZs.

In regions of increased turbidity (e.g., surf zones and river plumes), oil and sediment particles can mix, leading to the formation of oil-particle aggregates (OPAs) and ultimately providing a mechanism for depositing oil to the seabed (Daly et al., 2016). OPAs may become neutrally or negatively buoyant, meaning they can either suspend in the water column or sink to the seabed. Additionally, currents can carry them upward, as noted by Fitzpatrick et al., 2015.

Models for generating OPAs based on population balance equations incorporated in hydrodynamic models of river and estuarine flows have been made recently (Cui et al., 2021a, 2021b). Cui et al. (2021b) report on the implementation of an OPA model in a single water column model of a coastal ocean 140 m deep. Depth profiles of flow velocity and sediment and oil concentrations were prescribed from a 3D hydrodynamic model. Cui et al. (2021a) also developed a single water column model of OPA formation under the influence of prescribed analytical/empirical flow velocity and turbulent kinetic energy dissipation depth profiles, characteristic of an open channel (river) flow. Their OPA model consisted of the A-DROP model introduced earlier by Zhao et al. (2016). They report that small oil droplets that measured 50 μm were entrained in the water column at elevated turbulent kinetic energy dissipation rates. Meanwhile, larger droplets that measured 200 μm aggregated much faster.

This manuscript investigates full-depth LC as a mechanism that simultaneously entrains oil droplets and resuspends sediments, thereby promoting the formation of OPAs. A methodology is developed capable of (1) resolving full-depth LCs in an inner-shelf coastal ocean region unaffected by lateral boundaries and (2) modeling the formation of oil-particle OPAs induced by the cells. Towards this end, an OPA model based on population balance equations is coupled with the Reynolds-averaged Navier-Stokes equation governing the Langmuir cells flow. The transport of dispersed entities (e.g., oil, sediment, and OPAs) is simulated as passive scalars via the advection-diffusion equation. The model of Cui et al. (2021a), based on population balance equations, is used to account for the formation of OPAs.

The Reynolds-averaged formulation of LC flows proposed by Perez et al. (2021) is used to model a steady field of LS in a water column of $H = 15$ m depth formed by waves of intermediate wavelength $\lambda = 6H$, significant amplitude and period of 0.6 m and 8 s, respectively, and a wind stress of 0.1 N m^{-2}. These conditions were characteristic of the wind and wave forcing during the LS measurements of Gargett et al. (2004) in the passage of a storm. LC formation requires modeling the interaction between wind-driven shear current and Stoke drift shear (caused by surface gravity waves). Craik and Leibovich (1976) proposed a method for the formation of LC consisting of a vortex force (the Craik-Leibovich (C-L) vortex force) in the momentum equations, bypassing the need to resolve the surface gravity waves responsible for LC. The C-L vortex force is expressed as the cross-product of the Stokes drift velocity and vorticity, where the Stokes drift is defined in terms of the dominant wavelength and amplitude of the surface waves, and the local water column depth (Phillips, 1966). The Reynolds averaging solution strategy relies on the momentum equations with the C-L vortex force, while treating the largest, most coherent cells of the Langmuir turbulence (i.e., the field LS in this case) as a secondary component to the wind-driven shear mean flow. As the Reynolds-averaged formulation resolves the mean flow and the larger LC scales (i.e., the LS), it is equipped with a turbulence model that considers the smaller unresolved Langmuir scales (smaller than the LS).

2. Reynolds-averaged flow equations and turbulence model

The Reynolds-averaged Eulerian formulation proposed by Perez et al. (2021) is used in this study. The approach is both non-hydrostatic and incompressible, and consists of solving the Reynolds-averaged continuity and Navier-Stokes equation with the C-L vortex force:

$$\frac{\partial \langle u_i \rangle}{\partial x_i} = 0 \tag{1}$$

$$\frac{\partial \langle u_i \rangle}{\partial t} + \langle u_j \rangle \frac{\partial \langle u_i \rangle}{\partial x_j} = -\frac{1}{\rho}\frac{\partial \langle \Pi \rangle}{\partial x_i} + \nu \frac{\partial^2 \langle u_i \rangle}{\partial x_j^2} - \frac{\partial \left\langle u_i' u_j' \right\rangle}{\partial x_j} + \epsilon_{ijk} U_j^S \langle \omega_k \rangle \tag{2}$$

where $\langle\rangle$ indicate Reynolds averaging; $\langle u_i \rangle$ and $\langle \omega_i \rangle$ is the Reynolds-averaged velocity and vorticity component in the i^{th} direction, respectively; $\langle \Pi \rangle$ is a modified mean pressure; ρ is the density of seawater; ν is molecular kinematic viscosity; $\langle u_i' u_j' \rangle$ is the Reynolds stress; ϵ_{ijk} is the totally antisymmetric third-rank tensor; U_i^S is the Stokes drift velocity component in the i^{th} direction; x_i is the coordinate in the i^{th} direction (i.e., x_1-downwind, x_2-crosswind, and x_3-vertical directions); t is time. The Reynolds-averaged flow field $\langle u_i \rangle$consists of the mean wind-driven flow and the large-scale Langmuir turbulence (i.e., the LS). Meanwhile, the fluctuating components u_i' possess the smaller unresolved scales that

correspond to the unresolved Langmuir turbulence. The modified pressure $\langle\Pi\rangle$is defined by McWilliams et al. (1997) as:

$$\langle\Pi\rangle = \frac{\langle p\rangle}{\rho} + \frac{1}{2}\left[U_i^S U_i^S + 2\langle u_i\rangle U_i^S\right] \tag{3}$$

where $\langle p\rangle$ is the mean pressure.

The C-L vortex force, expressed as $\epsilon_{ijk}U_j^S\langle\omega_k\rangle$ in (2), is the cross product of the Stokes drift velocity and the mean vorticity. The waves generating LC are characterized by their dominant frequency (σ), wavenumber (k), and amplitude (a). The wave dispersion relation is utilized to relate k and σ. The wavenumber $k = 2\pi/\lambda$ is defined in terms of the dominant wavelength (λ). The Stokes drift velocity (Phillips, 1966) is expressed as:

$$U_i^S = \sigma k a^2 \frac{\cosh(2kx_3)}{2\sinh^2(kH)}\, n_i \tag{4}$$

where n_i is a unit vector representing the direction of the Stokes drift velocity; H is the water column depth. This study sets the stokes drift velocity in the downwind direction (i.e., $n_i = [1, 0, 0]$).

The Reynolds stress in Eq. (2) accounts for LC-induced non-local transport (Smyth et al., 2002; McWilliams et al., 2012; Harcourt, 2013; Sinha et al., 2015; Perez et al., 2021) and is modeled as:

$$-\left\langle u_i' u_j'\right\rangle = \nu_t\left(\frac{\partial < u_i >}{\partial x_j} + \frac{\partial < u_j >}{\partial x_i}\right) - \frac{2}{3}k\delta_{ij} + \nu_t\left(\frac{\partial U_i^S}{\partial x_j} + \frac{\partial U_j^S}{\partial x_i}\right) \tag{5}$$

where δ_{ij} is the Kronecker delta function which takes the value of one when subscript $i = j$, and zero otherwise; ν_t is the eddy viscosity that is calculated using the standard k-epsilon closure model:

$$\nu_t = C_\mu \frac{k^2}{\varepsilon} \tag{6}$$

where k is the turbulent kinetic energy (TKE) and ε the TKE dissipation rate. The standard k-epsilon model (Launder and Spalding,1974; Versteeg and Malalasekera, 2007) requires solving the transport equations for k and ε:

$$\frac{\partial k}{\partial t} + \langle u_j\rangle\frac{\partial k}{\partial x_j} = \frac{\partial}{\partial x_j}\left[\left(\nu + \frac{\nu_t}{\sigma_k}\right)\frac{\partial k}{\partial x_j}\right] + G_k - \varepsilon \tag{7}$$

$$\frac{\partial \varepsilon}{\partial t} + \langle u_j\rangle\frac{\partial \varepsilon}{\partial x_j} = \frac{\partial}{\partial x_j}\left[\left(\nu + \frac{\nu_t}{\sigma_\varepsilon}\right)\frac{\partial \varepsilon}{\partial x_j}\right] + C_{1\varepsilon}\frac{\varepsilon}{k}G_k + C_{2\varepsilon}\frac{\varepsilon^2}{k} \tag{8}$$

$$G_k = -\left\langle u_i' u_j'\right\rangle\frac{\partial\langle u_i\rangle}{\partial x_j} - \left\langle u_i' u_j'\right\rangle\frac{dU_j^S}{dx_i} \tag{9}$$

where G_k is the TKE production composed of production by mean shear and by Stokes drift shear Harcourt, 2013). The model constants (C_μ,σ_k, $C_{1\varepsilon}$and$C_{2\varepsilon}$) in Eqs. (6), ((7), and (8) have the following values $C_\mu = 0.09$, $\sigma_k = 1$, $\sigma_\varepsilon = 1.3$, $C_{1\varepsilon} = 1.44$ and $C_{2\varepsilon} = 1.92$ (Wilcox, 1994).

3. Oil-particle-aggregates model

The advection-diffusion equation and a population balance model are coupled to study the formation of OPAs due to mixing promoted by LS (see sketch in Fig. 2). The OPA model (OPAMOD) proposed by Cui et al. (2021b) represents the interactions between three dispersed entities: oil droplets, sediment flocs, and OPAs. Each entity has a set of classes assigned with a diameter, density, and settling or rising velocity. The entities were assumed to be spherical. The model considers fluid-sheared collisions between sediment flocs and oil droplets, OPAs and oil droplets, and sediment flocs and OPAs. The model neglects OPA breakup processes like other models (Zhao et al., 2016). This population balance model is a size-class-based model that calculates the number of particles by distributing mass among the fixed-size classes. It was assumed that OPAs exhibit fractal behavior similar to sediment flocs (Cui et al., 2021b). The effective density ρ_e for sediment floc and OPA was calculated with the following expression (Kranenburg, 1994):

$$\rho_e = (\rho_s - \rho_w)\left(\frac{D_p}{D}\right)^{3-nf} \tag{10}$$

where, ρ_s and D_p are the density and diameter of the primary particle; ρ_w is the density of seawater; D is the diameter; and n_f is the fractal dimension.

The advection-diffusion equations are used to simulate the movement of dispersed entities as passive tracers. Three entities are set: sediment flocs, oil droplets, and OPAs denoted by subscript (e) as *SED*, *OIL*, and *OPA*, respectively. The advection-diffusion equation for the volumetric concentration is expressed as:

$$\frac{\partial N_{e,m}}{\partial t} + \frac{\partial}{\partial x_i}\left(v_{e,m}N_{e,m}\right) - \frac{\partial}{\partial x_i}\left(D_t\frac{\partial N_{e,m}}{\partial x_i}\right) = L_{e,m} + G_{e,m} \tag{11}$$

where $N_{e,m}$ is the number concentration of the dispersed entity e of the m^{th} class; and $v_{e,m}$ is the velocity field. The transport of the dispersed entities due to turbulence is modeled with the eddy diffusivity term $D_t = \nu_t/S_c$; where ν_t is the eddy viscosity, and $S_c = 0.7$ is the turbulent Schmidt number. The variation in the number concentration due to mass exchanges between different classes is accounted for via the gain ($G_{e,m}$) and loss ($L_{e,m}$) terms. The model calculates and updates these source terms. Note that only OPA classes will have a non-zero gain term.

The dispersed entities are modeled as passive scalars, allowing them to follow the local flow. The velocity field ($v_{e,m}$) of the dispersed entity e

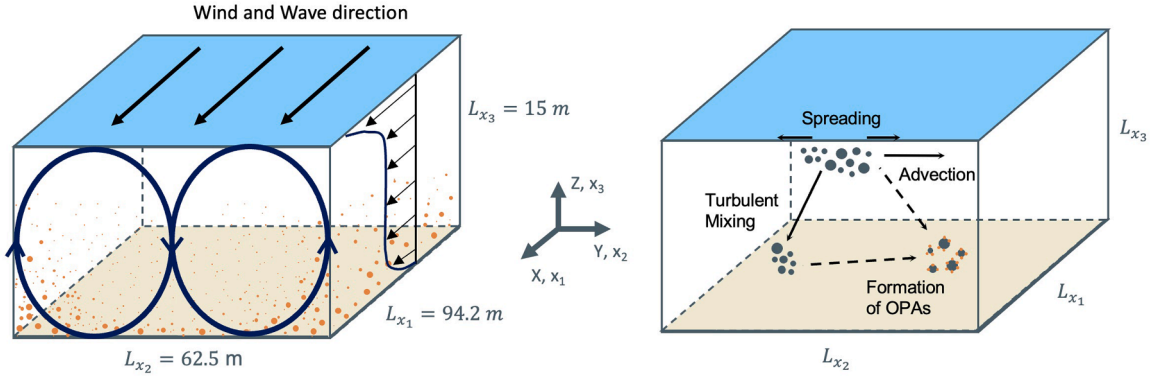

Fig. 2. (a) Sketch of uniform depth computational domain representative of a coastal ocean region unaffected by lateral boundaries following LES of Tejada-Martínez and Grosch (2007). Dark blue circles denote the expected orientation of Langmuir supercells. Orange circles represent the sediment flocs. (b) Sketch illustrating the mixing between oil and sediments, and eventually the OPA formation induced by the Langmuir cells.

of the m^{th} class is determined by:

$$v_{e,m} = \langle u_i \rangle + w_{e,m} n_i \tag{12}$$

where $\langle u_i \rangle$ is the local flow velocity; $w_{e,m}$ is the magnitude of the rise (oil) or settling (sediment flocs and OPAs) velocity of the m^{th} class; n_i is a unit vector representing the direction of the rising or settling velocity. In the adopted coordinate system (Fig. 2), $n_i = [0, 0, -1]$ for sediment and OPA classes, and $n_i = [0, 0, 1]$ for oil classes.

Ye et al. (2020) investigated OPA characteristics (size, effective density, and settling velocity) from oil-polluted bentonite clays. The OPA characteristics recorded in these experiments have been used here (Tables 1 and 2). The rising velocities for the oil classes (Table 3) were obtained via Raj (1977), assuming that oil droplets behave like solid spheres. The sediment, oil and OPA size classes in Tables 1–3 have been chosen following Cui et al. (2021b).

The following expressions account for the loss ($L_{OPA,m}$) and gain ($G_{opa,m}$) of OPA number concentration of the m^{th} class needed for Eq. (11) presented further above:

$$L_{OPA,\mathrm{m}} = -N_{OPA,m} \sum_{j=1}^{n_{oil}} \alpha A_{mj} N_{OIL,\,j} - N_{OPA,m} \sum_{j=1}^{n_{sed}} \alpha A_{mj} N_{SED,\,j} \tag{13}$$

$$G_{OPA,\mathrm{m}} = \sum_{i=1}^{n_{oil}} \sum_{j=1}^{n_{sed}} \alpha A_{ij} N_{OIL,i} N_{SED,\,j} + \sum_{i=1}^{m-1} \sum_{j=1}^{n_{sed}} \alpha A_{ij} N_{OPA,i} N_{SED,\,j} + \sum_{i=1}^{n_{oil}} \times \sum_{j=1}^{m-1} \alpha A_{ij} N_{OIL,i} N_{OPA,\,j} \tag{14}$$

where α denotes the collision efficiency. The collision probability A_{ij} between two colliding entities of diameters D_i and D_j is specified as:

$$A_{ij} = \frac{1}{6} G \left(D_i + D_j\right)^3 \tag{15}$$

where G is the turbulent shear rate, defined as $G = \sqrt{\varepsilon/\nu}$. Overall, the formation of OPAs is proportional to A_{ij}. Furthermore, a high turbulent shear rate G increases the collision probability, thus inducing greater OPA formation.

Sediment gain is strictly limited to the erosion flux boundary condition to be described further below. Furthermore, in the case study presented further below, a non-uniform sediment concentration field is imposed and held static in OPAMOD; thus, sediment losses are neglected. This is based on the assumption that any sediment loss due to aggregation with oil is immediately replaced, as the seabed serves as a continuous sediment source.

The loss term for oil classes is expressed by:

$$L_{OIL,m} = -N_{OIL,m} \sum_{j=1}^{n_{sed}} \alpha A_{mj} N_{SED,\,j} - N_{OIL,m} \sum_{j=1}^{n_{opa}} \alpha A_{mj} N_{OPA,\,j} \tag{16}$$

The model tracks a fixed set of OPA classes, each classified with density, settling velocity, and diameter. The collision of two components, such asoil from the i^{th} – class of mass $m_{OIL,i}$ andsediment from the j^{th} – class of mass $m_{SED,j}$, forms OPA with a resulting mass of $m_{OPA,k} = m_{OIL,i} + m_{SED,j}$. Assuming that $m_{OPA,k}$ falls between two adjacent OPA classes, $m_{OPA,k}$ is distributed linearly between those two adjacent classes (Verney et al., 2011; Cui et al., 2021b).

A flux boundary condition is specified at the surface and bottom (seabed) for all dispersed entities (SED, OIL, and OPA):

$$N_{e,m} w_{e,m} n_3 - D_t \frac{\partial N_{e,m}}{\partial x_i} = q_{e,m} \tag{17}$$

where $q_{e,m}$ is the flux at the corresponding boundary for dispersed entity e of the m^{th} class. At the surface, a zero-flux ($q_{e,m} = 0$) boundary condition is imposed for all entities (SED, OIL, and OPA). At the bottom, a zero-flux ($q_{OIL,m} = 0$) boundary condition is imposed for OIL. For sediment flocs, the bottom flux is set as an erodible and depositional boundary (Warner et al., 2008; Cheng et al., 2015; Liu et al., 2019; Yue et al., 2020):

$$q_{SED,m} = q_{d,m} + q_{r,m} \tag{18}$$

where $q_{r,m}$ and $q_{d,m}$ are the erosion and deposition flux, respectively. The deposition flux $q_{d,m}$ is modeled as $q_{d,m} = w_{e,m} n_3 N_{e,m}$. OPAs are deposited on the seabed via the settling velocity, so a depositional boundary is implemented ($q_{OPA,m} = q_{d,m}$). The sediment erosion flux $q_{r,m}$ is calculated following Ariathurai and Arulanandan (1978):

$$q_{r,\mathrm{m}} = \begin{cases} E_0 (1 - \varphi) \dfrac{\tau - \tau_{cr,m}}{\tau_{cr,m}} & \left(\tau \geq \tau_{cr,m}\right) \\ 0 & \left(\tau < \tau_{cr,m}\right) \end{cases} \tag{19}$$

The bed erodibility was set $E_0 = 5x10^{-4} kgm^{-2}s^{-1}$(Liu et al., 2019), and porosity was taken as $\varphi = 0.5$ (Warner et al., 2008). Critical shear stress ($\tau_{cr,m}$) values based on the currents are reported in Table 4 following the Shields curve reported in Soulsby et al. (1997). The critical shear stress could also take into account the wave activity but was not incorporated for simplicity.

The present study investigates the vertical mixing of oil droplets as they get entrained into the water column. Lateral spreading of the oil by the action of the cells is not considered. Thus, the oil is initially set at the surface above the LS downwelling limb, simulating a field of oil droplets having been already aligned along the surface convergences of the cells, forming oil slicks (i.e. windrows). Thus, periodicity is specified in the crosswind and downwind directions for all entities (SED, OIL, and OPA). This approach was also followed by Perez et al. (2021) in their Lagrangian simulation of oil droplets in a field of LS.

4. Computational setup

The proposed framework is applied to a shallow water wind and wave-driven flow of uniform depth, representing an inner-shelf coastal ocean region unaffected by lateral boundaries. This formulation follows the LES of Tejada-Martínez and Grosch (2007) and the Reynolds-averaged simulation of Perez et al. (2021). The domain is set to model a pair of full-depth LC (see sketch in Fig. 2), coherent along the downwind direction, as reported in the field measurements of Gargett et al. (2004). The domain lengths are: $L_{x_1} = 94.2$ m, $L_{x_2} = 62.8$ m, and $L_{x_3} = 15$ m. The domain is represented by a structured (uniform) hexahedral mesh with 4 elements in x_1 (downwind), 64 elements in x_2 (crosswind), and 96 elements in x_3 (vertical). Only 4 elements are chosen in the downwind direction given that the cells are strongly coherent in that direction and do not show any variation in that direction once the solution reaches steady state.

The case is initialized from rest. The top boundary is set as a wind-sheared rigid lid. The velocity profile in Fig. 2 shows the primary flow direction. The shear stress is set equal to 0.1 N m^{-2}. The bottom is a no-slip boundary with a roughness of 1 mm. Periodicity is specified in the

Table 1
Diameter (D, μm) for sediment (SED), OPA, and OIL classes following Ye et al. (2020).

	1	2	3	4	5	6	7	8	9	10	11	12
SED	30	60	100	140	180							
OPA	30	60	100	140	180	220	280	360	440	520	600	680
OIL	40	60	80	120	120	140						

crosswind and downwind directions.

Langmuir cells can be characterized by two dimensionless parameters: the ratio of wavelength to depth λ/H and the turbulent Langmuir number La_t. The latter, representative of the strength of wind forcing relative to wave forcing, is defined as $La_t = \sqrt{u_\tau/u_S}$ (McWilliams et al., 1997), where u_τ is the wind stress friction velocity and $u_S$is a characteristic Stokes drift velocity. A flow with $La_t < 1$ is dominated by wave forcing over wind forcing. The velocities in the expression for La_t are defined as $u_\tau = \sqrt{\tau_{wind}/\rho}$ and $u_S = \sigma k a^2$, where τ_{wind} is the wind stress. For the given wind and wave forcing conditions discussed earlier observed during the Gargett et al. (2004) measurements of LS in the field, $\tau_{wind} = 0.1$ N m^{-2}, $\lambda/H = 6$, $k = 2\pi/\lambda$, $a = 0.6$m, and with σ obtained from the dispersion relation, $La_t = 0.7$.

The continuity and momentum Eqs. (1)-(2), the turbulence model Eqs. (7)-(8), and the scalar transport Eq. (11) were solved with a finite volume method on a staggered grid to ensure the coupling between pressure and velocity (Patankar, 1980). The momentum, turbulent kinetic energy, and turbulent dissipation rate equations implemented a second-order upwind scheme. The scalar transport equations utilized the Quadratic Upstream Interpolation for Convective Kinematics (QUICK) scheme.

The solution strategy for the Langmuir cell-OPA coupled model is as follows. First, a steady-state full-depth LS solution is obtained as previously described. This is proceeded by running the sediment transport (advection-diffusion) equations subject to the steady state LS flow, leading to a steady state solution for sediment concentration. It is assumed that the sediment used to generate OPAs is immediately replenished via Langmuir cell suspension, as described earlier. Thus the advection-diffusion equation for the m^{th} sediment can be written as follows.

$$\frac{\partial}{\partial x_i}\left(\langle u_i\rangle N_{SED,m}\right) + w_{SED,m} n_3 \frac{\partial N_{SED,m}}{\partial x_3} - \frac{\partial}{\partial x_i}\left(D_t \frac{\partial N_{SED,m}}{\partial x_i}\right) = 0 \; m = 1,\ 2,\ \cdots, 5 \tag{20}$$

The steady-state sediment solution is used as a static input to the OPA model to generate OPAs from the sediments (assuming continuous replenishment of sediments) and a finite amount of oil released at the surface. The advection-diffusion equations with the population balance presented in (11)–(14) are shown below for oil and OPA:

$$\frac{\partial N_{OIL,m}}{\partial t} + \frac{\partial}{\partial x_i}\left(\langle u_i\rangle N_{OIL,m}\right) + w_{OIL,m} n_3 \frac{\partial N_{OIL,m}}{\partial x_3} - \frac{\partial}{\partial x_i}\left(D_t \frac{\partial N_{OIL,m}}{\partial x_i}\right) = -N_{OIL,m}\sum_{j=1}^{n_{sed}} \alpha A_{mj} N_{SED,\,j} - N_{OIL,m}\sum_{j=1}^{n_{opa}} \alpha A_{mj} N_{OPA,\,j} \; m = 1,\ 2,\ \cdots, 6 \tag{21}$$

$$\begin{aligned}\frac{\partial N_{OPA,m}}{\partial t} + \frac{\partial}{\partial x_i}\left(\langle u_i\rangle N_{OPA,m}\right) + w_{OPA,m} n_3 \frac{\partial N_{OPA,m}}{\partial x_3} - \frac{\partial}{\partial x_i}\left(D_t \frac{\partial N_{OPA,m}}{\partial x_i}\right) \;&= -N_{OPA,m}\sum_{j=1}^{n_{oil}} \alpha A_{mj} N_{OIL,\,j} - N_{OPA,m}\sum_{j=1}^{n_{sed}} \alpha A_{mj} N_{SED,\,j} + \sum_{i=1}^{n_{oil}}\sum_{j=1}^{n_{sed}} \alpha A_{ij} N_{OIL,i} N_{SED,\,j} \\ &+ \sum_{i=1}^{m-1}\sum_{j=1}^{n_{sed}} \alpha A_{ij} N_{OPA,i} N_{SED,\,j} + \sum_{i=1}^{n_{oil}}\sum_{j=1}^{m-1} \alpha A_{ij} N_{OIL,i} N_{OPA,\,j} \; m = 1,\ 2,\ \cdots, 12\end{aligned} \tag{22}$$

Note that $w_{OPA,m} n_3 < 0$ and $w_{OIL,m} n_3 > 0$. The fractal dimension n_f and collision efficiency $\alpha$was 0.35 and 2.3, respectively. Both values are reported and validated by Cui et al., 2021b via a zero-dimensional simulation matching the laboratory results by Ye et al. (2020). This simulation is tested in this study, further details are given in the Appendix.

A finite amount of oil droplets is released at the surface with a spill size $\Delta x_2 = 20m$. The oil spill center location is above the LS downwelling limb. For each oil class, a uniform mass concentration of 0.1 kg m^{-3} was set on the cells adjacent to the surface. Oil concentration thresholds were set. The oil-particle aggregation process was active when oil concentration were above 0.001 kg m^{-3} (Cui et al., 2021b).

Table 3
Rising velocity (w_r,mms^{-1}) for OIL classes (Raj, 1977).

	1	2	3	4	5	6
OIL	0.0675	0.142	0.250	0.390	0.564	0.783

Table 4
Critical shear stress ($\tau_{cr,m}$, Pa) for sediment (SED) classes (Soulsby et al., 1997).

	1	2	3	4	5
SED	0.0599	0.0434	0.0343	0.0295	0.0263

5. Reynolds averaged resolved flow

The Reynolds-averaged solution from (1)-(2), re-expressed as $u_i^{RANS} = \langle u_i\rangle$, can be decomposed into a primary and secondary component as $u_i^{RANS} = \langle u_i\rangle_{x_1,x_2} + v_i^{RANS}$; where $\langle u_i\rangle_{x_1,x_2}$ is the steady state u_i^{RANS} solution averaged in the downwind and crosswind directions; and v_i^{RANS} is the LS-induced fluctuation. The latter may be obtained as $v_i^{RANS} = u_i^{RANS} - \langle u\rangle_{x_1,x_2}$ for post-processing.

The LS structure can be seen in Fig. 3(a)-(c) in terms of the resolved LS-induced velocity fluctuation v_i^{RANS}. Panel (a) shows the upwelling and downwelling limbs of the LS. Regions of negative vertical velocity engulfing the water column reveal the downwelling limb. In contrast, full-depth regions of positive velocity reveal the upwelling limb. Panel (b) depicts the surface convergence of the LS in terms of crosswind velocity, indicating the top of the downwelling region. Panel (c) shows the downwind LS-induced velocity fluctuation, represented by a near-bottom intensification, a binding signature of LS (Gargett et al., 2004; Gargett and Wells, 2007), coinciding with the downwelling limb.

The solution of the turbulence model is shown in Fig. 3(d)-(e) in terms of TKE and TKE dissipation rate. The highest values of the TKE dissipation rate ε occur at the surface and the bottom, especially in the downwelling region. The turbulent shear rate is spatially non-uniform

Table 2
Settling velocity (w_s,mms^{-1}) for sediment (SED) and OPA classes (Ye et al., 2020).

	1	2	3	4	5	6	7	8	9	10	11	12
SED	0.135	0.480	1.105	1.480	1.886							
OPA	0.433	0.597	0.725	1.459	2.186	2.873	3.673	5.497	7.087	8.348	13.696	11.003

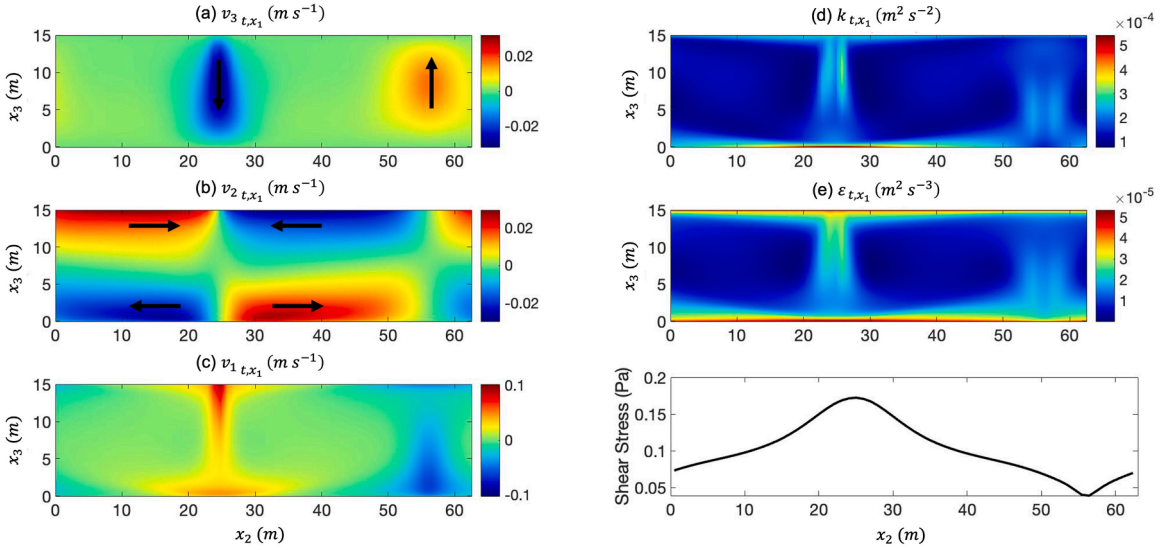

Fig. 3. Resolved steady-state LS-induced velocity fluctuation v_i^{RANS}displayed on the crosswind-vertical (x_2-x_3) plane, panels (a)-(c). In panel (a), the arrows pointing downwards and upwards represent the cell's dowelling and upwelling limbs, respectively. In panel (b), the arrows pointing to the right and left indicate the cell's surface convergence and bottom divergence. Panels (d)-(e) are contours of the turbulent kinetic energy TKE (k, m^2s^{-2}) and TKE dissipation rate (ε, m^2s^{-3}). Note that panel (e) has been log-scaled. Panel (f) plots the bottom shear stress (Pa) along the crosswind direction.

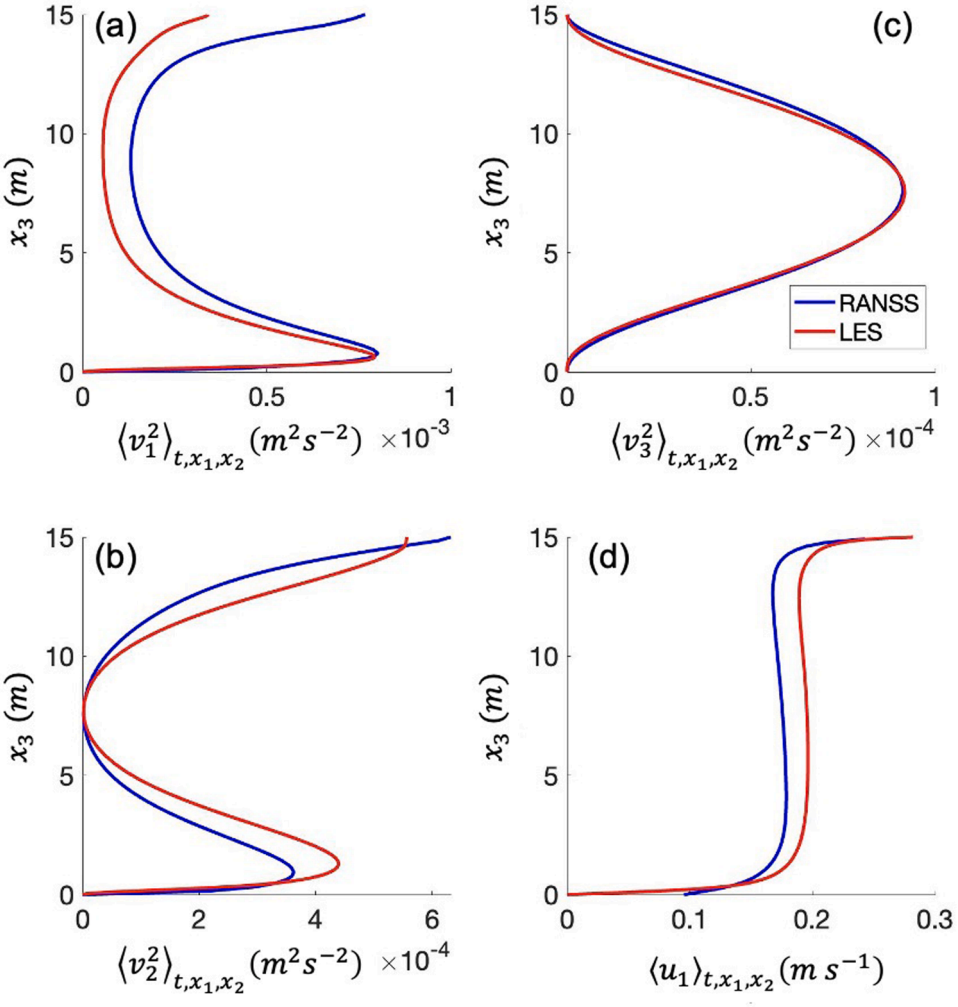

Fig. 4. Velocity variance induced by LS resolved via RANSS (shown in blue) compared to an LES (shown in red), panels (a)-(c). Mean downwind velocity profile, panel (d).

and is in the same order as the LES of Liu et al. (2019). Recall that this parameter defines the shear rate ($G = \sqrt{\varepsilon/\nu}$) in the OPA model.

Fig. 3(f) shows the shear stress at the bottom. Note that for a wind stress $\tau_{wind} = 0.1$ Pa applied as the surface, the resulting bottom shear stress modulated by the Langmuir cell will result in sediment erosion and suspension (see Table 4). The bottom shear stress varies around the fixed wind stress value. The downwelling limb leads to a thinning of the bottom boundary layer and, thus, a local increase in bottom shear stress. The upwelling limb of the cell leads to a thickening of the bottom boundary layer and, thus, a local decrease in bottom shear stress. This behavior is essential for the sediment lift caused by the Langmuir cells.

In Fig. 4, depth profiles of LS-induced velocity v_i^{RANS} variances obtained are compared to the LES of Tejada-Martinez and Grosch (2007) executed with a mesh of 32 × 64 × 96 cells. The LS structure is consistent in both solutions. The downwind velocity variance in Fig. 4(a) shows an intensification near the seabed, a key feature of LS. The crosswind velocity variance (Fig. 4(b)) reveals an intensification at the surface caused by the surface convergence of LS. Based on the profiles, the RANS formulation could benefit from more accurate calibration of the turbulence model coefficients to better align the results with the LES. Note that there is a significant difference in computing cost. The LES on 16 parallel processors takes approximately one week to run, whereas the RANS simulation or RANSS on a single-core desktop takes about one hour.

6. Oil-particle-aggregates formation and transport

The result for the steady state sediment solution is shown in Fig. 5. Note that the erosion of sediments induced by the LS and the settling velocity of the sediment leads to a steady-state (equilibrium) solution. The smaller sediments are more uniformly throughout the LS structure and show a greater number concentration. The larger sediments remain closer to the bottom, primarily suspended within the upwelling limb of the cells. The bottom convergence zone of the full-depth cells sweeps the suspended sediments, ultimately collecting them within the upwelling limb. Thus, the upwelling limb coincides with a higher concentration of suspended sediments.

Fig. 6 shows the vertical profiles of suspended-sediment concentrations in terms of mass concentration averaged in the downwind and crosswind directions, with the higher concentrations corresponding to the smaller sediment particles.

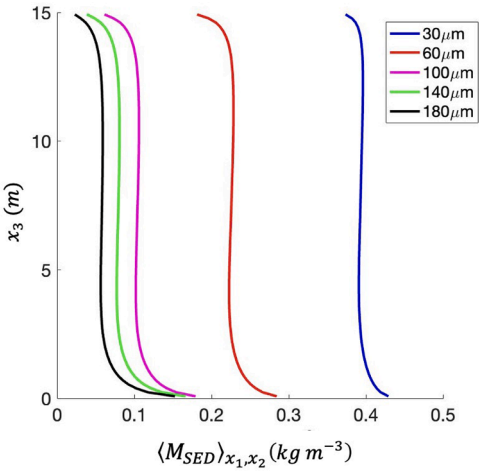

Fig. 6. Vertical profiles of suspended sediment concentrations averaged over the streamwise and spanwise directions ($\langle M_{SED} \rangle_{x_1,\ x_2}$).

As for the OPA model, it is assumed that the sediment used to generate OPAs is immediately replenished via Langmuir cell suspension. Thus, the steady-state sediment concentration solution previously shown is held static and inputted into the OPA model. A finite amount of oil droplets was released on the surface, corresponding to a spill size of $\Delta x_2 = 20m$ above the downwelling limb. A mass concentration of 0.1 kg m^{-3} was applied to each oil class to the cells neighboring the surface.

Figs. 7 and 8 show the spatial-temporal distribution of oil droplets displayed over the crosswind-vertical plane for oil classes C1 (40μm) and C6 (140μm), respectively. By 500 s (~8 mins.), the available oil has been trapped in OPAs. This is indicated by the time series of the percentage of unaggregated oil shown in Fig. 9. The larger oil classes are consumed more rapidly near the surface, e.g., C6 (140μm) is consumed within 40 s. Recall that oil-particle aggregation was only active if oil concentrations were above 0.001 kg m^{-3}. Thus, the percentages of unaggregated oil shown in Fig. 9 do not reach zero.

The panels in Figs. 10–12 show the spatio-temporal evolution of the OPA concentrations for classes C2 (60μm), C7 (280μm), and C12 (680μm), respectively. The OPAs are seen to evolve as a cloud, initially forming at the surface, with the cloud then being swept down by the cell

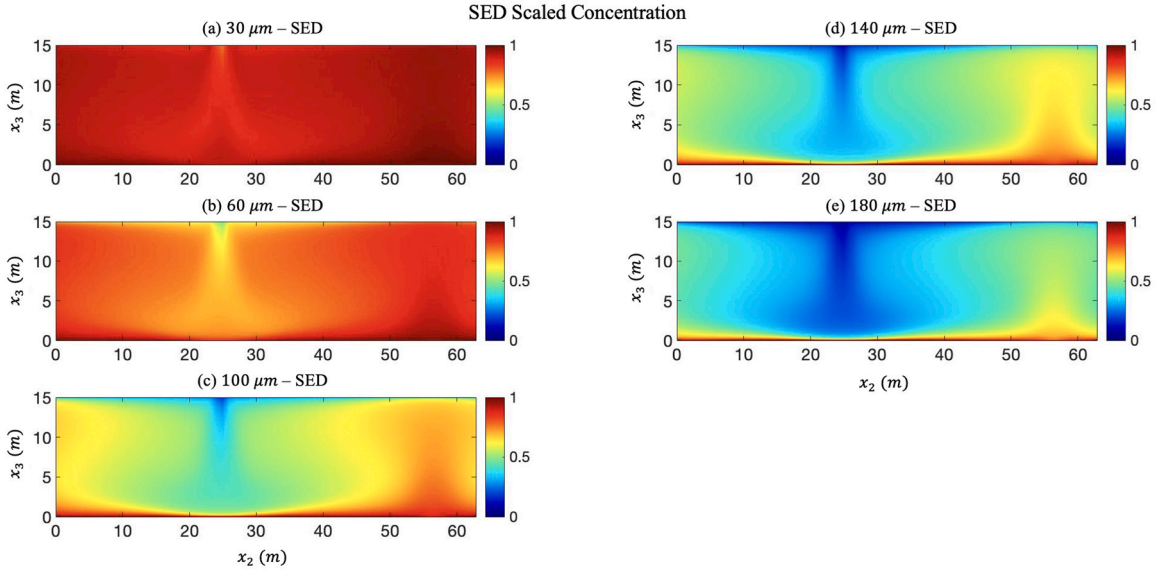

Fig. 5. Spatial distribution of sediment flocs (SED) displayed on the crosswind-vertical (x_2-x_3) plane. Concentrations have been scaled by the maximum concentration for each class.

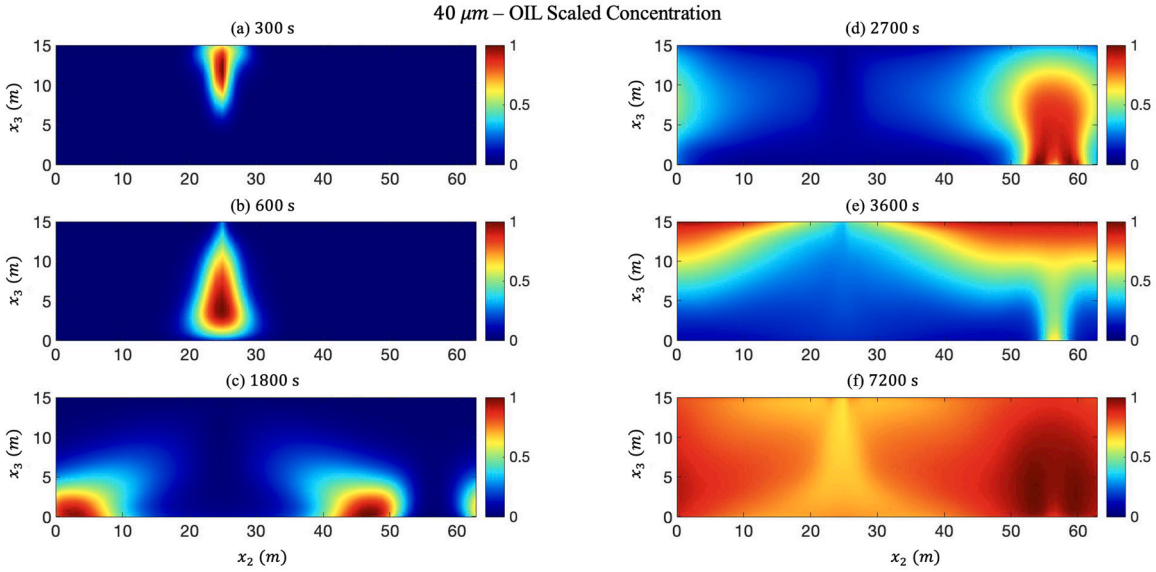

Fig. 7. Spatial-temporal distribution of oil droplets displayed on the crosswind-vertical (x_2-x_3) plane for oil class C1(40μm) at simulation time: (a) 300 s; (b) 600 s; (c) 1800s; (d) 2700s; (e) 3600 s; (f) 7200 s. Concentrations have been scaled by the maximum concentration at the corresponding time.

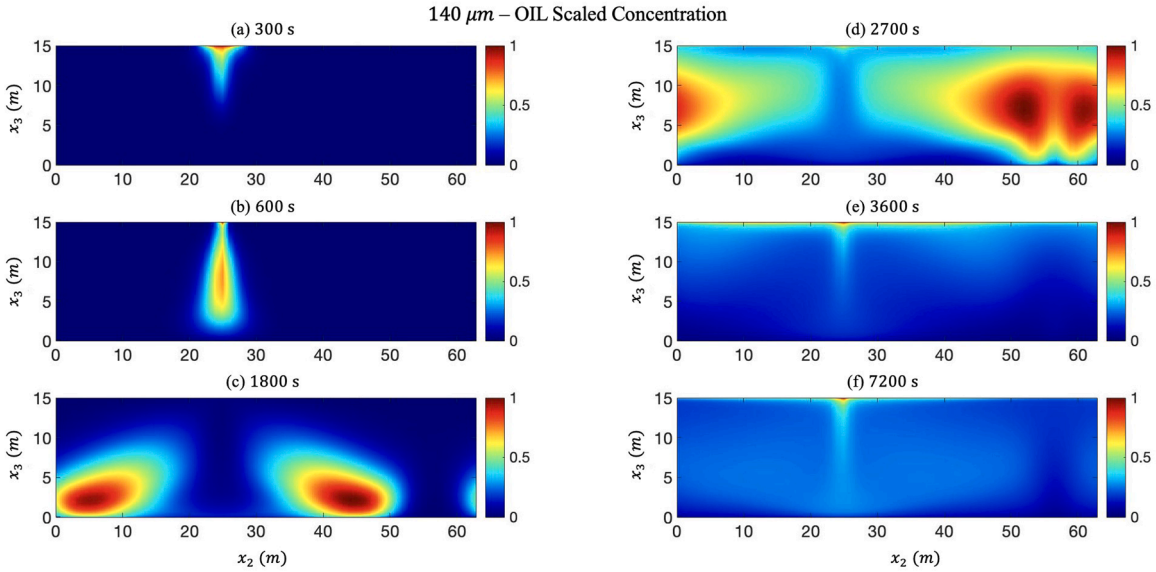

Fig. 8. Spatial-temporal distribution of oil droplets displayed on the crosswind-vertical (x_2-x_3) plane for oil class C6 (140μm) at simulation time: (a) 300 s; (b) 600 s; (c) 1800s; (d) 2700s; (e) 3600 s; (f) 7200 s. Concentrations have been scaled by the maximum concentration at the corresponding time.

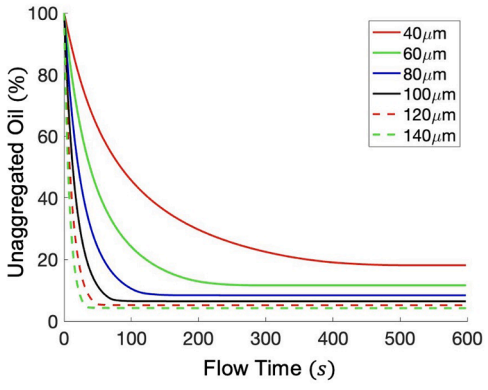

Fig. 9. Time series of percentage of unaggregated oil (C1-C6).

while growing and eventually splattering at the bed and splitting into two clouds. In particular, the clouds of the larger OPAs quickly come to near rest, suspended within the upwelling limbs of the Langmuir cells at depths where these OPAs are close to being neutrally buoyant. The clouds eventually settle slowly to the bottom over periods longer than the simulation.

Fig. 13 shows time series of volume averaged OPA concentrations. Note the significant spike in OPA concentration that occurs by about 600 s, shown in panel (b). This can be attributed to the initial downward transport of OPAs by the downwelling limb of the LS (seen e.g. in Figs. 10–12 at 600 s) followed by the upward transport by the upwelling limb (seen in Figs. 10–12 at 1800s). Throughout this path, the volume-averaged OPA concentrations first decrease (for the lower-mid-size classes) or become almost stagnant (for the higher-size classes) over time, due to deposition of OPAs at the bed. However, the OPA concentrations eventually start to increase as the OPAs that remain suspended

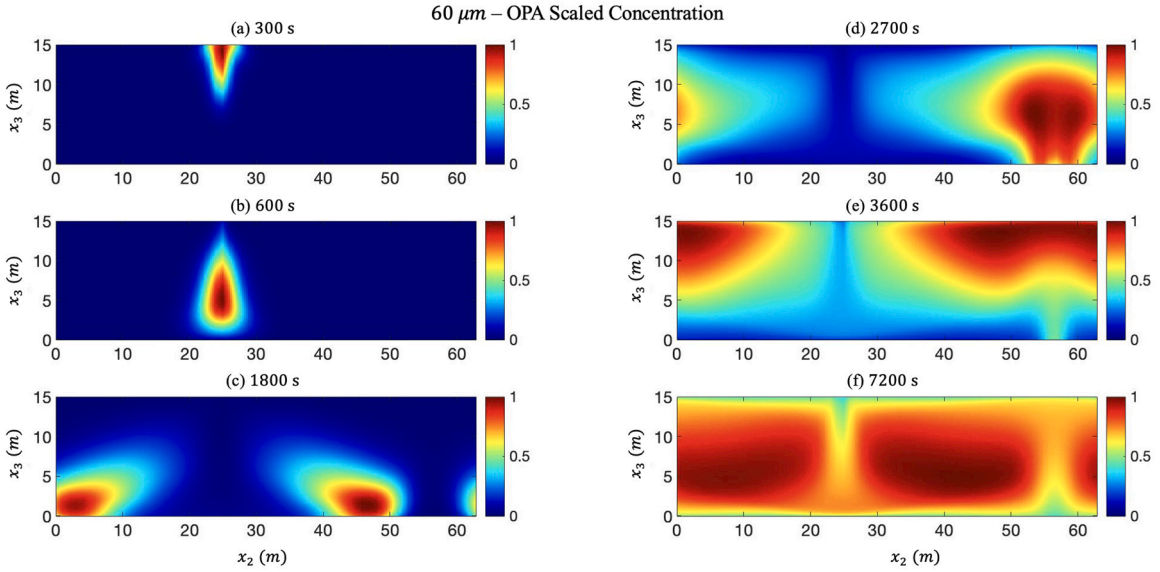

Fig. 10. Spatio-temporal evolution of the OPA concentrations displayed on the crosswind-vertical (x_2-x_3) plane for OPA class C2 (60 μm) at simulation time: (a) 300 s; (b) 600 s; (c) 1800s; (d) 2700s; (e) 3600 s; (f) 7200 s. Concentrations have been scaled by the maximum concentration at the corresponding time.

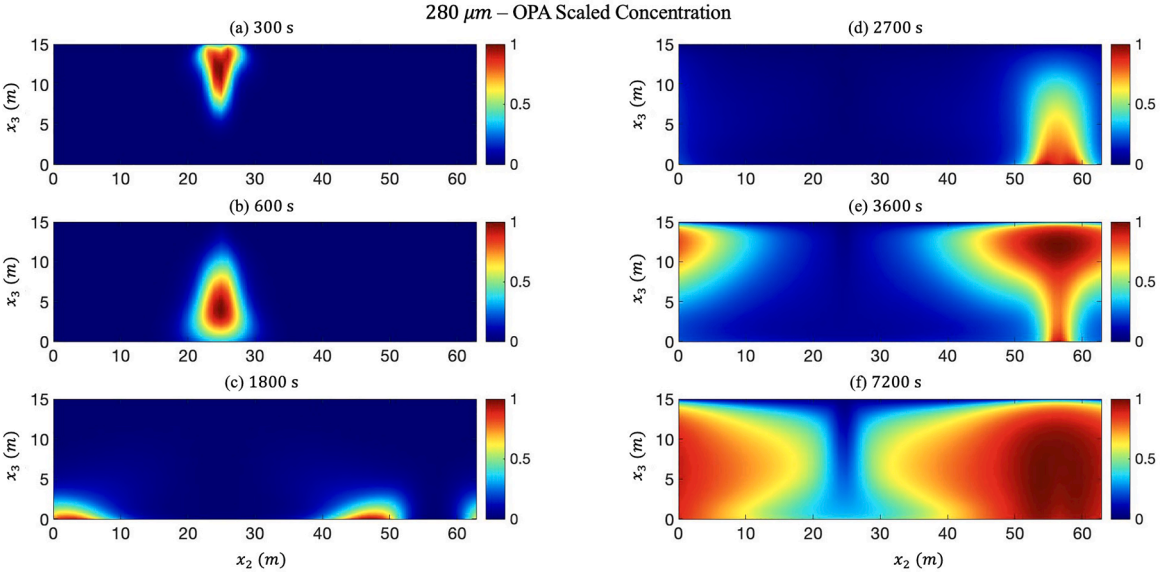

Fig. 11. Spatio-temporal evolution of the OPA concentrations displayed on the crosswind-vertical (x_2-x_3) plane for OPA class C7 (280 μm) at simulation time: (a) 300 s; (b) 600 s; (c) 1800s; (d) 2700s; (e) 3600 s; (f) 7200 s. Concentrations have been scaled by the maximum concentration at the corresponding time.

come into contact with sediments populating the upwelling limb of the LS. The upwelling limbs carry high sediment concentrations, thereby leading to the second peak in OPA formation, observed in Fig. 13(b). The secondary peak is also due to the smaller OPAs evolving into larger OPAs as they collide with the constantly replenished sediments.

Looking at the volume-averaged mass concentration time series in Fig. 13(a), large and medium size OPA classes (in the range 180–360 and 440–680 μm, respectively) accumulate more mass than the smaller OPA classes (30–140 μm). At about 2000s, OPA formation favored the medium size classes, with number concentrations about 2.5 times greater than that of large size classes. However, this trend changed, as by about 5000 s, the large size OPAs had accumulated more mass, about 2 times greater than medium size OPAs. Similar conclusions can be made from Fig. 14, which shows depth profiles of OPA concentrations at various times.

Small-size classes show small mass concentration throughout the simulation. Comparing peaks in Fig. 13(a), the large class is about 20 times larger, and the medium class is about 10 times larger.

OPAs form at the surface as soon as the oil was released there mainly because of the larger oil droplets at the surface aggregating with the smaller sediment particles that are initially present near the surface (see the static distribution of sediments inputted to the OPA model in Fig. 5). Thus, these larger droplets are not transported to the bottom by the cell, as they become quickly trapped in OPAs. This explains why the percentage of unaggregated larger droplets decays quicker, as shown in Fig. 9. Conversely, the smaller oil droplets are swept down by the cells before there is time for them to get trapped in the lighter sediments near the surface. As such, these smaller oil droplets survive for a more extended period, eventually getting trapped in OPAs by the heavier sediments. This explains why the unaggregated percentage of the smaller oil droplets decays slower than that of the larger oil droplets, as seen in Fig. 9.

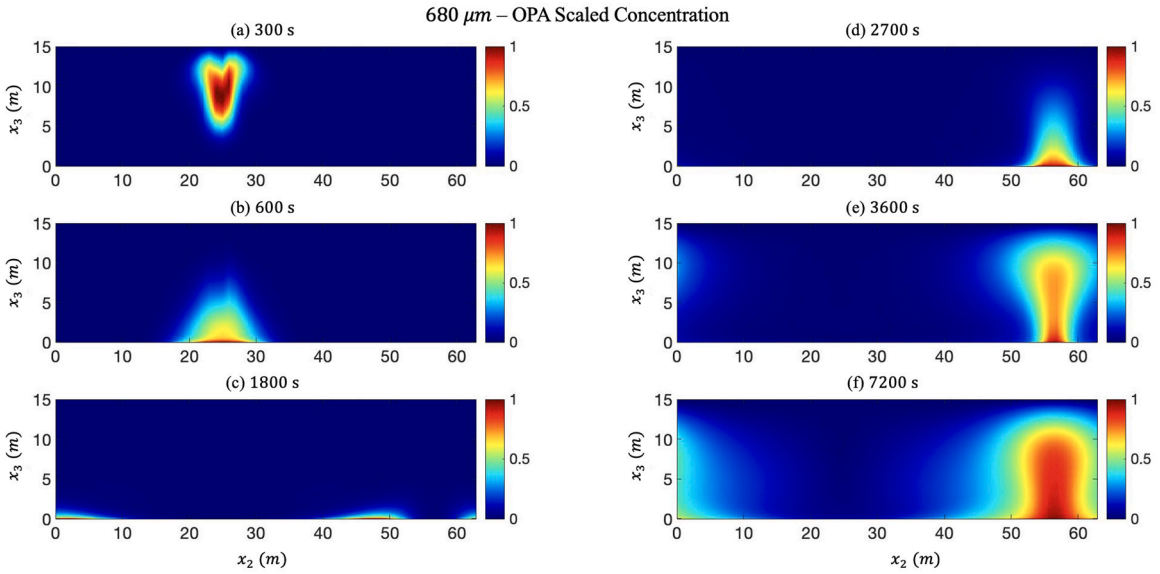

Fig. 12. Spatio-temporal evolution of the OPA concentrations displayed on the crosswind-vertical (x_2-x_3) plane for OPA class C12 (680 μm) at simulation time: (a) 300 s; (b) 600 s; (c) 1800s; (d) 2700s; (e) 3600 s; (f) 7200 s. Concentrations have been scaled by the maximum concentration at the corresponding time.

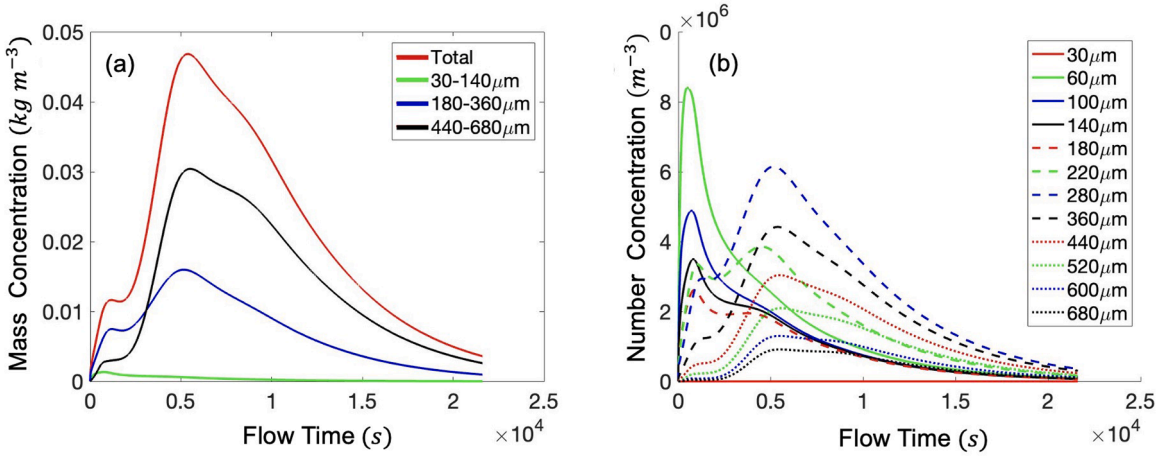

Fig. 13. (a) Time series of volumed averaged mass concentration of OPAs: Total (C1-C12), small size (C1-C4), medium size (C4-C8), large size (C8-C12). (b) Time series of volumed averaged number concentration of OPAs (C1-C12).

Recall that the rate of OPA formation is proportional to the cube of sediment diameter plus oil diameter, seen through the A_{ij} tensor in (15). Thus, the fact that near the surface, the lighter oil becomes trapped in OPAs at a relatively slow rate (because of the smaller sediments there) allows their unaggregated percentage to remain higher for a longer time.

In addition to being dependent on oil and sediment particle diameters, the rate of OPA formation is proportional to the turbulent shear rate $G = \sqrt{\varepsilon/\nu}$, as can be seen through (14). In Fig. 3(e), it is seen that LS induces a spatially non-uniform rate of OPA formation through the non-uniform spatial distribution of TKE dissipation rate (ε). For example, LS brings about relatively high values of ε within its downwelling limb as well as near the surface and the bottom of the water column. Thus, through its spatial distribution of TKE and TKE dissipation, LS plays an important factor in determining the rate of OPA formation, in addition to determining the spatial distribution of OPAs.

7. Conclusion

A Reynolds-averaged formulation was introduced, resolving the mean wind and wave-driven shear flow plus the most significant scale of the Langmuir turbulence corresponding to full-depth LC or LS. This steady flow was used to track the formation of OPAs induced by Langmuir cells mixing sediments and oil. This was accomplished by coupling an OPA model based on population balance equations with the Reynolds-averaged equations governing the LS flow. The simulation presented exhibited the entrainment and general distributions of sediment flocs, oil droplets, and OPAs influenced by LS over time in a water column of 15m depth. The flow was driven by the wind and wave forcing conditions measured by Gargett et al. (2004) in their field measurements of LS during the passage of a storm.

In the Reynolds-averaged simulation performed, the erosion of sediments and sediment settling velocity lead to a steady-state (equilibrium) solution of sediment concentration. The LS-modulated bottom shear stress was sufficiently high to induce sediment erosion, with sediments subsequently distributed in the water column via the vertical transport provided by the upwelling and downwelling limbs of the LS. Smaller sediments were more evenly suspended throughout the water, while larger sediments stayed closer to the bottom within the upwelling limb of the LS. When oil was released at the surface, OPAs formed on the surface due to the aggregation of larger oil droplets with smaller

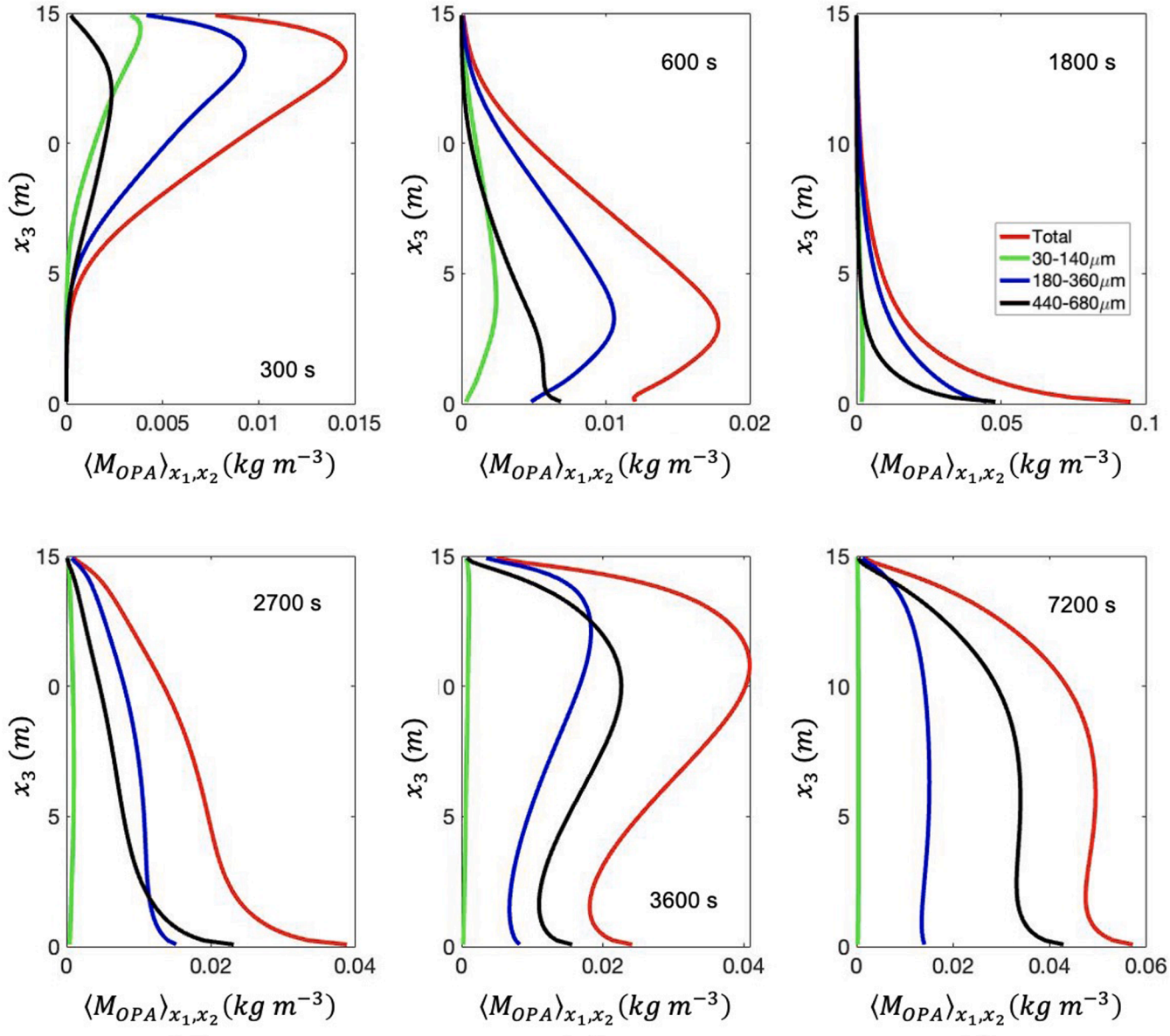

Fig. 14. Vertical profiles of OPA concentrations averaged over the streamwise and spanwise directions ($\langle M_{OPA}\rangle_{x_1,\ x_2}$) at simulation time: (a) 300 s; (b) 600 s; (c) 1800s; (d) 2700s; (e) 3600 s; (f) 7200 s.

sediment particles already present. Smaller oil droplets were observed to survive longer as they first were submerged by the downwelling limb, with the majority eventually becoming trapped in OPAs as they were carried upward by the upwelling limb of the LS.

The formation of OPAs starts as a cloud on the surface that is swept down by the cell as the cloud grows. The cloud then splatters at the bed and divides into two clouds. Larger OPAs quickly come to rest and are suspended within the upwelling limbs of the Langmuir cells at depths where they are almost neutrally buoyant. These clouds settle slowly to the bottom.

The results obtained here suggest that full-depth LC can be a significant driver of sediment resuspension and OPA formation in coastal regions. As such, LC may serve as an important mechanism for preventing oil from washing out at the shore and instead remain buried at the seabed. In the future, hydrodynamic models of the coastal ocean circulation should consider this mechanism to predict the fate and transport of spilled oil more accurately.

The OPA formation model implemented does not consider the breakup of oil droplets and OPAs. Oil droplets and OPAs may break up due to a high local energy dissipation rate (Cui et al., 2021c; Ji et al., 2023). The RANS simulations with the present k-epsilon model may not be able to reproduce the high local energy dissipation generated by winds and waves. However, it is worth mentioning that the k-epsilon model may be modified to account for wave breaking (Uchiyama et al., 2010; Paskyabi and Fer, 2014; Moghimi et al., 2016). Furthermore, Cui et al., 2021c have shown that turbulence can be strong enough to cause a breakup of oil droplets into smaller ones, and Ji et al. (2023) show that suspended sediments in coastal environments can pierce oil droplets and OPAs, resulting in smaller particles. Thus, the OPA model should be updated to account for these processes during the presence of Langmuir supercells.

It is well-known that LCs lead to the formation of oil slicks along the surface convergences of the cells. A key finding of the manuscript, which had not been considered before, is that the oil droplets can be entrained into the water column via LC downwells while mixing with sediments suspended in the water column by the action of LC upwells, forming OPAs that will eventually reach and settle on the seabed. This represents a previously unidentified mechanism that could potentially contribute

to the formation of tar mats buried in the sea floor (Warnock et al., 2015). Consequently, in the event of an oil spill under LC conditions, the response should include the recovery of oil not only from the water column but also from the seabed.

CRediT authorship contribution statement

J.J. Peñaloza-Gutierrez: Conceptualization, Methodology, Software, Validation, Visualization, Writing – original draft, Writing – review & editing. **A.E. Tejada-Martínez:** Conceptualization, Methodology, Supervision, Project administration, Funding acquisition, Visualization, Writing – original draft, Writing – review & editing. **M.C. Boufadel:** Conceptualization, Methodology, Supervision.

Declaration of Competing Interest

The authors declare that they have no known competing financial interests or personal relationships that could have appeared to influence the work reported in this paper.

Data availability

Data will be made available on request.

Acknowledgment

This research was supported by a grant from the Gulf of Mexico Research Initiative.

Appendix

The experiments conducted by Ye et al. (2020) and the zero-dimensional model by Cui et al. (2021b) were used to validate the OPA model. Ye et al. (2020) investigated the characteristics of OPAs formed from crude oil mixed with bentonite clay. To generate OPAs, 1.0 g of oil and 0.5 g of clay were combined in a container with 1.0 L of synthetic seawater. The components were mixed at 490 rpm for 2 h (equivalent TKE dissipation rate ε of 0.02 m^2 s^{-3}) and then allowed to settle.

As reported by Cui et al. (2021b), a zero-dimensional model was configured to simulate the experiment. The settling/rising velocities are not considered. The shear rate $G = 20\ s^{-1}$ is held constant for 2 h of simulation time, reproducing the experiment conditions. The sediment floc, oil-particle aggregate, and oil classes are listed in Table 1. The collision efficiency and fractal dimension used in the simulation were obtained from Cui et al. (2021b).

The resolved size distribution by the model (Fig. A1) shows an adequate agreement with Ye et al. (2020). The modeled OPA number peaked for class 6 (220 μm), accounting for ~18 % of the population. In comparison, the experimental OPA number peaked for class 5 (180 μm) with ~20 % of the population. Overall, OPAs were predominantly made up of small and medium-sized aggregates, with over 95 % of the population falling into this category (Fig. A1b).

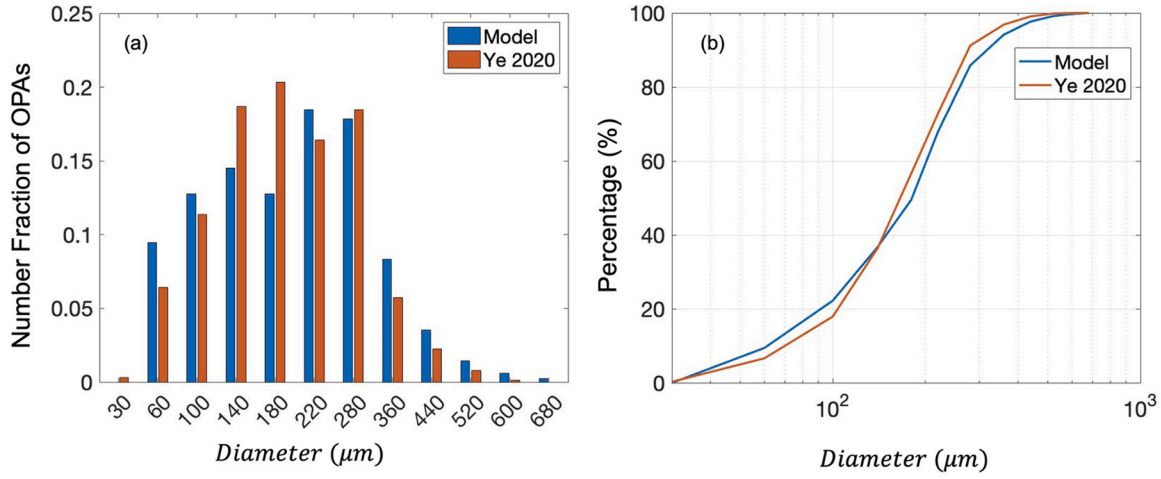

Fig. A1. Comparison between the laboratory experiments (Ye et al., 2020) and zero-dimensional model: (a) histogram of the OPA number fraction and size classes, (b) cumulative number percentage of OPAs.

References

Ariathurai, R., Arulanandan, K., 1978. Erosion rates of cohesive soils. J. Hydraul. Div. 104 (2), 279–283.
Cheng, Z., Yu, X., Hsu, T.J., Ozdemir, C.E., Balachandar, S., 2015. On the transport modes of fine sediment in the wave boundary layer due to resuspension/deposition: a turbulence-resolving numerical investigation. J. Geophys. Res. Oceans 120 (3), 1918–1936.
Chubarenko, I., Stepanova, N., 2017. Microplastics in Sea Coastal ZONE: lessons learned from the Baltic amber. Environ. Pollut. 224, 243–254.
Craik, A.D.D., Leibovich, S., 1976. A rational model for Langmuir circulation. J. Fluid Mech. 73, 401–426.
Cui, F., Daskiran, C., Lee, K., Boufadel, M.C., 2021a. Transport and formation of OPAS in Rivers. J. Environ. Eng. 147 (5), 04021012.
Cui, C., Harris, C.K., Tarpley, D.R., 2021b. Formation of oil-particle-aggregates: numerical model formulation and calibration. Front. Mar. Sci. 8, 629476.
Cui, F., Behzad, H., Geng, X., Zhao, L., Lee, K., Boufadel, M.C., 2021c. Dispersion of oil droplets in Rivers. J. Hydraul. Eng. 147 (3), 04021004.
Daly, K.L., Passow, U., Chanton, J., Hollander, D., 2016. Assessing the impacts of oil-associated marine snow formation and sedimentation during and after the deepwater Horizon oil spill. Anthropocene 13, 18–33.
Farmer, D., Li, M., 1994. Oil dispersion by turbulence and coherent circulations. Ocean Eng. 21, 575–587.
Fitzpatrick, F.A., Boufadel, M.C., Johnson, R., Lee, K.W., Graan, T.P., Bejarano, A.C., et al., 2015. Oil-Particle Interactions and Submergence from Crude Oil Spills in Marine and Freshwater Environments: Review of the Science and Future Research Needs. USGS, Reston, VA. Open-File Report.
Gargett, A.E., Wells, J.R., Tejada-Martínez, A.E., Grosch, C.E., 2004. Langmuir supercells: a mechanism for sediment resuspension and transport in shallow seas. Science 306, 1925–1928.

Gargett, A.E., Wells, J.R., 2007. Langmuir turbulence in shallow water. Part I. Observations. J. Fluid Mech. 576, 27–61.
Harcourt, R.R., 2013. A second-moment closure model of Langmuir turbulence. J. Phys. Oceanogr. 43, 673–697.
Ji, W., Abou-Khalil, C., Parameswarappa Jayalakshmamma, M., Boufadel, M., Lee, K., 2023. Post-formation of oil particle aggregates: breakup and biodegradation. Environ. Sci. Technol. 57 (6), 2341–2350.
Kranenburg, C., 1994. The fractal structure of cohesive sediment aggregates. Estuar. Coast. Shelf Sci. 39, 451–460.
Langmuir, I., 1938. Surface motion of water induced by wind. Science 87, 119–123.
Launder, B.E., Spalding, D.B., 1974. The numerical computation of turbulent flows. Comput. Methods Appl. Mech. Eng. 3 (2), 269–289.
Liu, J., Liang, J., Xu, K., Chen, Q., Ozdemir, C.E., 2019. Modeling sediment flocculation in Langmuir turbulence. J. Geophys. Res. Oceans 124 (11), 7883–7907.
McWilliams, J.C., Sullivan, P.P., Moeng, C.H., 1997. Langmuir turbulence in the ocean. J. Fluid Mech. 334, 1–30.
McWilliams, J.C., Huckle, E., Liang, J., Sullivan, P., 2012. The wavy Ekman layer: langmuir circulations, breakers, and Reynolds stress. J. Phys. Oceanogr. 42, 1793–1816.
Moghimi, S., Thomson, J., Özkan-Haller, T., Umlauf, L., Zippel, S., 2016. On the modeling of wave-enhanced turbulence nearshore. Ocean Model. 103, 118–132.
Paskyabi, M., Fer, I., 2014. Turbulence structure in the Upper Ocean: a comparative study of observations and modeling. Ocean Dyn. 64 (4), 611–631.
Patankar, S.V., 1980. Numerical Heat Transfer and Fluid Flow. Hemisphere Publishing Corporation, Washington, USA.
Perez, A.J., Cui, F., Peñaloza-Gutierrez, J.J., Zeidi, S., Sinha, N., Boufadel, M.C., Smith, C., Murphy, D.W., Tejada-Martínez, A.E., 2021. Simulation of vertical dispersion of oil droplets by Langmuir supercells through a Reynolds-averaged Eulerian formulation combined with lagrangian particle tracking. Ocean Eng. 235, 109043.
Phillips, O.M., 1966. The Dynamics of the Upper Ocean. Cambridge University Press, Cambridge.
Raj, P.K., 1977. Theoretical Study to Determine the Sea State Limit for the Survival of Oil Slicks on the Ocean. Dept. of Transportation, Coast Guard, Office of Research and Development, Washington.
Savidge, D.K., Gargett, A.E., 2017. Langmuir supercells on the middle shelf of the South Atlantic bight: 1. Cell structure. J. Mar. Res. 75 (2), 49–79.
Sinha, N., Tejada-Martínez, A.E., Akan, C., Grosch, C.E., 2015. Toward a K-Profile Parameterization of Langmuir Turbulence in Shallow Coastal Shelves. J. Phys. Oceanogr. 45, 2869–2895.
Skyllingstad, E.D., Denbo, D.W., 1995. An ocean large-eddy simulation of Langmuir circulations and convection in the surface mixed layer. J. Geophys. Res. 100 (C5), 8501–8522.
Smyth, W., Skyllingstad, E., Crawford, G., Wijesekera, H., 2002. Non-local fluxes and Stokes drift effects in the K-profile parameterization. Ocean Dyn. 52, 104–115.
Soulsby, R., Whitehouse, R., 1997. Threshold of sediment motion in coastal environments. In: 13th Australasian Coastal and Ocean Engineering Conference and the 6th Australasian Port and Harbour Conference, 1. Centre for Advanced Engineering, University of Canterbury, pp. 145–150.
Stommel, H., 1949. Trajectories of small bodies sinking slowly through convection cell. J. Mar. Res. 8, 24–29.
Tejada-Martínez, A.E., Grosch, C.E., 2007. Langmuir turbulence in shallow water: Part II. Large-eddy simulation. J. Fluid Mech. 576, 63–108.
Thorpe, S.A., 2004. Langmuir circulation. Annu. Rev. Fluids Mech. 36, 55–79.
Uchiyama, Y., McWilliams, J.C., Shchepetkin, A.F., 2010. Wave–current interaction in an oceanic circulation model with a vortex-force formalism: application to the surf zone. Ocean Model. 34 (1–2), 16–35.
Verney, R., Lafite, R., Brun-Cottan, J.C., Le Hir, P., 2011. Behaviour of a floc population during a tidal cycle: laboratory experiments and numerical modeling. Cont. Shelf Res. 31, S64–S83.
Versteeg, H.K., Malalasekera, W., 2007. An Introduction to Computational Fluid Dynamics: The Finite Volume Method. Pearson Education.
Warner, J.C., Sherwood, C.R., Signell, R.P., Harris, C.K., Arango, H.G., 2008. Development of a three-dimensional, regional, coupled wave, current, and sediment-transport model. Comput. Geosci. 34 (10), 1284–1306.
Warnock, A.M., Hagen, S.C., Passeri, D.L., 2015. Marine tar residues: a review. Water Air Soil Pollut. 226 (3), 68.
Wilcox, D., 1994. Turbulence Modeling for CFD, 2nd ed. DCW Industries, Inc., La Cañada, CA, USA.
Ye, L., Manning, A.J., Hsu, T.J., 2020. Oil-mineral flocculation and settling velocity in saline water. Water Res. 173, 115569.
Yue, L., Cheng, Z., Hsu, T., 2020. A turbulence-resolving numerical investigation of wave-supported gravity flows. J. Geophys. Res. Oceans 125 (2), e2019JC015220.
Zhao, L., Boufadel, M.C., Geng, X., Lee, K., King, T., Robinson, B.H., et al., 2016. A-DROP: a predictive model for the formation of oil particle aggregates (OPAs). Mar. Pollut. Bull. 106, 245–259.